

# 1 **Nonlinear optical Hall effect in the Weyl semimetal WTe<sub>2</sub>**

2 Young-Gwan Choi<sup>1†</sup>, Manh-Ha Doan<sup>1†</sup>, Youngkuk Kim<sup>2,3</sup>, and Gyung-Min Choi<sup>1,3\*</sup>

3  
4 <sup>1</sup> Department of Energy Science, Sungkyunwan University, Suwon 16419, Korea

5 <sup>2</sup> Department of Physics, Sungkyunwan University, Suwon 16419, Korea

6 <sup>3</sup> Center for Integrated Nanostructure Physics, Institute for Basic Science, Suwon 16419, Korea

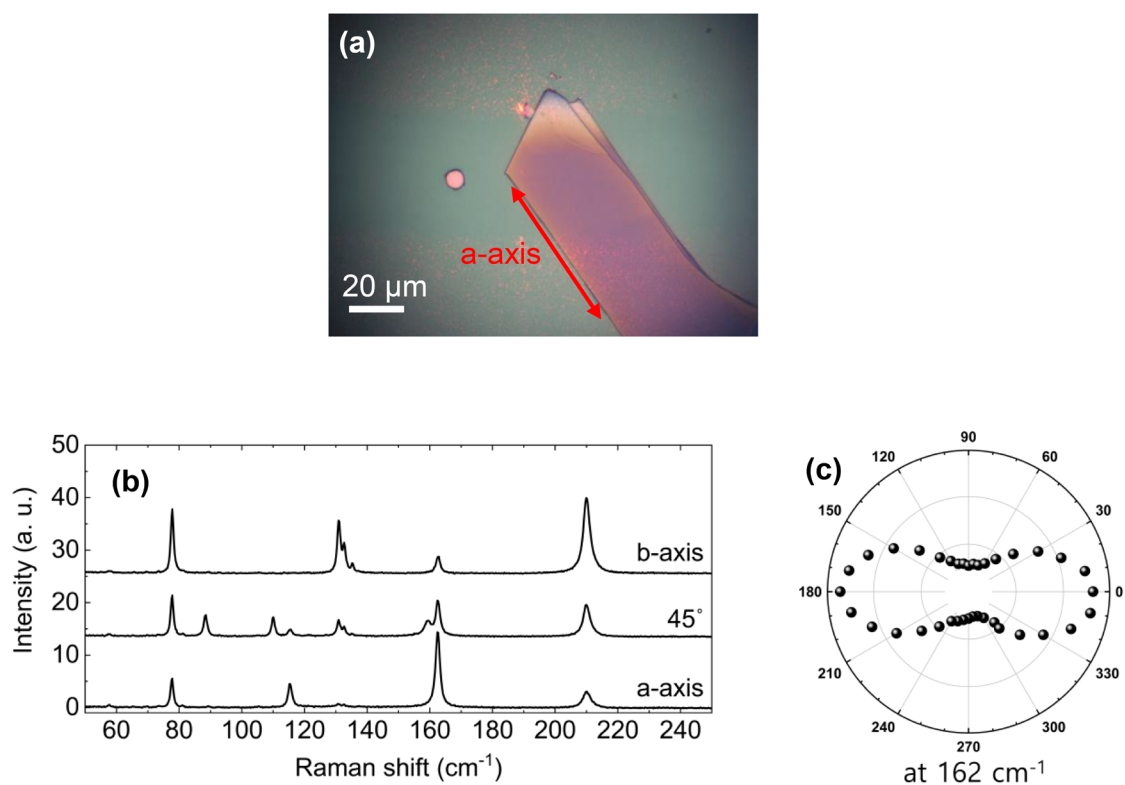
7  
8 †These authors contribute equally

9 \*E-mail: gmchoi@skku.edu

## 10 11 **S1. Definition of the crystal orientation of WTe<sub>2</sub> by polarized Raman spectroscopy**

12 Polarized Raman spectroscopy is a well-known technique to determine the crystallographic  
13 orientation of the asymmetry layered materials. For WTe<sub>2</sub>, the Raman peak at the center  
14 wavenumber of 162 cm<sup>-1</sup> is maximized when light polarization direction is parallel with the a-  
15 axis<sup>1,2</sup>. The Raman measurements were performed by using a confocal micro-Raman system  
16 at room temperature with the excitation source of the 1.96 eV (632.8 nm) line of a He-Ne laser.  
17 A 50x objective lens (0.8 NA) was used to focus the laser beam onto the sample and to collect  
18 the scattered light (backscattering geometry). The Raman signal was dispersed with a HORIBA  
19 iHR 550 spectrometer (2400 grooves per mm) and detected with a liquid-nitrogen-cooled back-  
20 illuminated charge-coupled-device (CCD) detector. The laser power was kept 0.3 mW. All  
21 measurements were conducted in the parallel-polarization configuration, where the analyzer  
22 angle was set such that photons with the polarization parallel to the incident polarization pass  
23 through. Another achromatic half-wave plate was placed in front of the spectrometer to keep  
24 the polarization direction of the signal entering the spectrometer constant with respect to the  
25 groove direction of the grating. Fig. S1 shows the polarized Raman results for our multilayer  
26 WTe<sub>2</sub> exfoliated on SiO<sub>2</sub>/Si substrates. Consistently with the previous reports<sup>1,2</sup>, we observe  
27 that the a-axis is always along the well-defined edge, which is naturally formed after exfoliation  
28 processes.

29



30

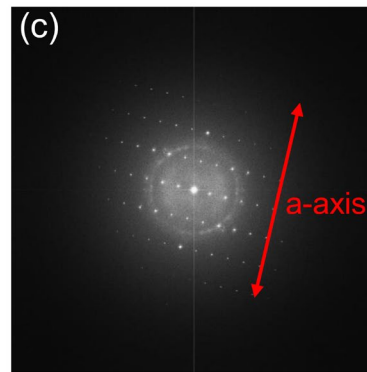
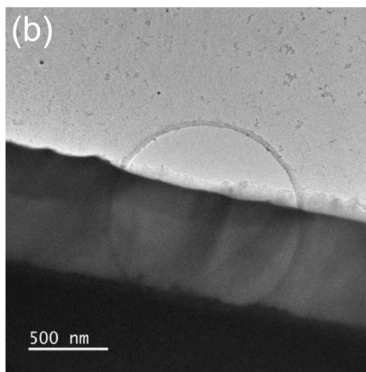
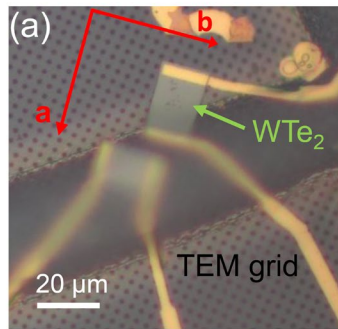
31

32 **Figure S1.** (a) Optical microscopy image of the multilayer WTe<sub>2</sub> flake, (b) Raman spectra with three different  
 33 light polarization angles, along the a-axis, 45° to a-axis, and the b-axis. (c) Polarization dependence of intensities  
 34 of the 162-nm peak. It shows the maximum peak value along a-axis.

35

36 **S2. Confirmation of the crystal orientation of the fabricated WTe<sub>2</sub> device by TEM**  
37 **measurements**

38 Because the crystal orientation of the investigated device is a critical factor for understanding  
39 mechanism of the nonlinear Kerr effect in our study. After all electrical and optical  
40 measurements, we conduct the TEM observations to reconfirm the crystal axis of the WTe<sub>2</sub>  
41 device. To transfer the WTe<sub>2</sub> device on SiO<sub>2</sub>/Si substrate to the TEM grid, poly (methyl  
42 methacrylate) (PMMA C4, MicroChem) is coated onto samples as a supporting layer and then  
43 immersed into a diluted hydrofluoric (HF) acid solution for etching the SiO<sub>2</sub> layer. The PMMA-  
44 supported device is then transferred to the TEM grids (PELCO, 200 mesh, copper, 1.2- $\mu$ m  
45 holes). And the PMMA layer is finally removed by acetone. TEM images is taken by using a  
46 probe aberration-corrected JEM ARM 200F system, operated at 80 keV. As presented in Fig.  
47 S2, our TEM observations show that the a- and b-axis of the fabricated device are well  
48 perpendicular with the CrAu electrodes and are consistent with the results in the polarized  
49 Raman spectroscopy above.

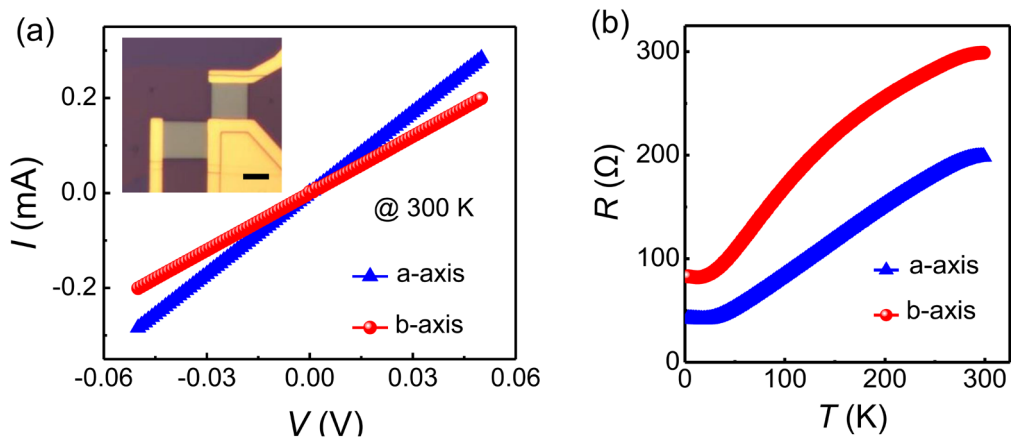


50  
51 **Figure S2.** (a) Optical microscopy image of the WTe<sub>2</sub> device transferred on the TEM grid. (b) TEM image and  
52 (c) its corresponding Fourier transformation (FFT) pattern. The a- and b-axis of the fabricated device are well  
53 perpendicular with the CrAu electrode and consistent with the observation in the polarized Raman spectroscopy  
54 above.

56 **S3. Metallic behavior and resistivity anisotropy of the WTe<sub>2</sub> devices**

57 Current-voltage characteristics of our fabricated devices at room temperature show a good  
58 conductivity of semi-metallic WTe<sub>2</sub> with the clear linear behavior as show in Fig. S3 (a). To  
59 further confirm its metallic property, we also conduct the electrical transport at low temperature.  
60 As presented in Fig.S3(b), both a- and b-axis devices show decreases of the resistance as  
61 temperature is decreased. The resistance anisotropy ratio between the a- and b-axis directions  
62 at 300 K is about 1.5.

63



64

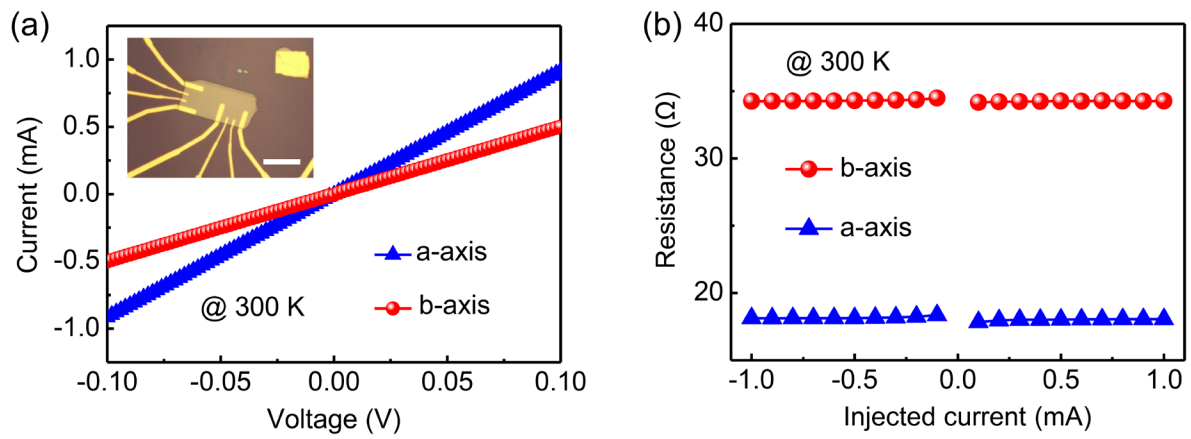
65 **Figure S3.** (a) Current-voltage characteristics of the investigated WTe<sub>2</sub> devices at room temperature. The inset its  
66 optical microscopy image. The scale bar presents 10 μm. (b) Temperature dependence of the 2-probe resistance  
67 of the device. The resistance anisotropy ratio between the a- and b-axis directions at 300 K is about 1.5.

68

69

70 To confirm the anisotropy of the bulk resistivity of WTe<sub>2</sub>, we fabricate additional WTe<sub>2</sub> devices  
71 and conduct the 4-probe resistance measurements for both the a- and b-axis directions within  
72 the sample multilayer flake. The 4-probe resistance anisotropy is around 1.9 as in Fig. S4 (b),  
73 which is in the similar range with the 2-probe resistance ratio of the device used for the Kerr  
74 effect measurements in the main text. The bulk resistivity along the a- and b-axis directions are  
75 calculated to be around 123.4 and 233.2 μΩ.cm, respectively.

76



77

78 **Figure S4.** (a) Current-voltage characteristics of the WTe<sub>2</sub> devices at room temperature. The inset its optical  
 79 microscopy image. The scale bar presents 20 μm (b) 4-probe resistances of the devices at room temperature. The  
 80 resistance anisotropy ratio between the a- and b-axis directions is about 1.9.

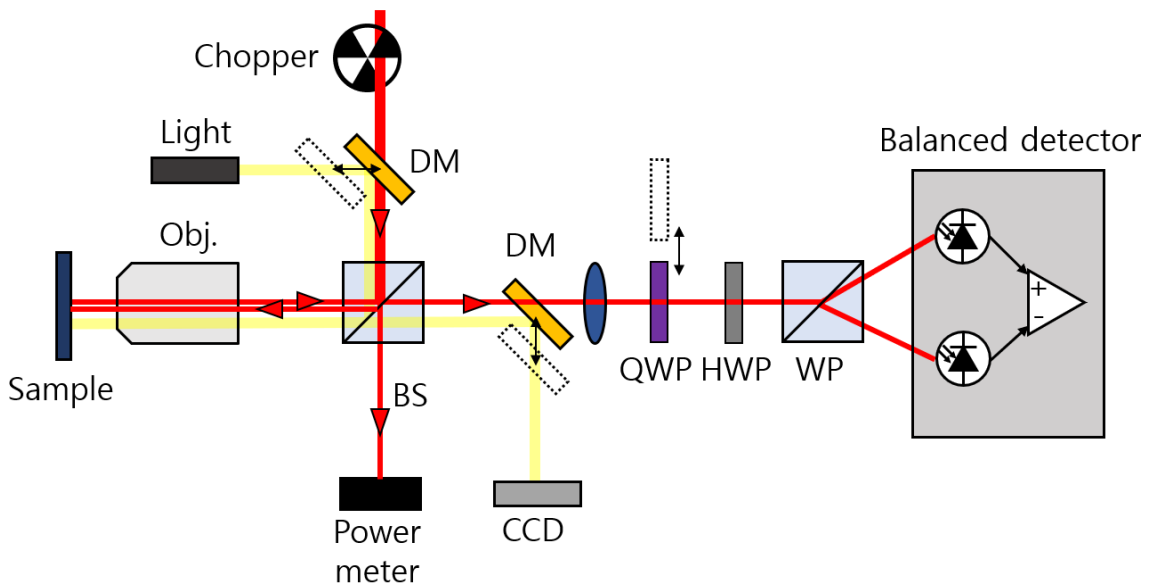
81

82

83 **S4. Schematic illustration of current-induced Kerr effect measurement setup**

84 AC current induced Kerr effect measurement setup was utilized for detecting polarization  
85 variation. A Ti:Sapphire oscillator generate pulse train with 785 nm center wavelength. A  
86 current source is utilized for alternating electric field to WTe<sub>2</sub> devices with 3 kHz modulation  
87 frequency. Laser beam is tightly focused on WTe<sub>2</sub> devices by passing through x50 objective  
88 lens. For grazing angle experiments, sample surface plane is tilted along vertical and horizontal  
89 direction and reflected beam is collected by the same objective lens. Beam radius is about 1  
90 μm, and power is about 5 mW. For adjusting light polarization direction, a half-wave plate  
91 (HWP1) was used. After reflection from the sample, laser beam was passing through the other  
92 half-wave plate (HWP2). Depending on the measurement configuration, a quarter-wave plate  
93 is positioned before HWP2 or not. Balanced detector and lock-in amplifier are used for  
94 observing subtle change of polarization of reflected light resulting from alternating current.  
95 The amplitude of electric field  $D_b$  is calibrated based on Ohm's law as,  $D_b = j_c \rho_b$ , where  $j_c$   
96 is current density ( $I/A$ ),  $\rho_b$  is resistivity along b-axis, A is cross-sectional area of the channel,  
97  $A = wt$ ,  $w$  is the channel width, and  $t$  is the thickness of the flake.  $I = 2$  mA,  $w = 13$  μm,  $t =$   
98 60 nm and  $\rho_b = 233.2$  μΩ · cm.

99



100

101 **Figure S5.** Schematic picture of AC current-induced Kerr effect measurement system. Obj. is objective lens, BS  
102 is 5:5 beam splitter, HWP is half-wave retarder plate, QWP is quarter-wave retarder plate, and WP is Wollaston  
103 prism.

104

105 **S5. Kerr angle expressions for anisotropic material**

106 For anisotropic system, we can put permittivity tensor as,

$$\varepsilon = \begin{bmatrix} \varepsilon_{xx} & \varepsilon_{xy} \\ \varepsilon_{yx} & \varepsilon_{yy} \end{bmatrix}. \quad (\text{S1})$$

107 For this permittivity tensor, refractive index and electric field can be written as<sup>3</sup>,

$$n_{\pm}^2 = \varepsilon_{\pm} = \frac{1}{2} \left( \varepsilon_{xx} + \varepsilon_{yy} \mp \sqrt{4\varepsilon_{xy}\varepsilon_{yx} + (\varepsilon_{xx} - \varepsilon_{yy})^2} \right). \quad (\text{S2})$$

108 Electric field can be described as  $\beta_{\pm} = \frac{E_y}{E_x}$  where  $\beta_+ = -\frac{\varepsilon_{yx}}{\delta}$  and  $\beta_- = -\frac{\delta}{\varepsilon_{xy}}$ . Then,

109 reflection matrix can be written as,

$$\begin{bmatrix} r_{xx} & r_{xy} \\ r_{yx} & r_{yy} \end{bmatrix} = \begin{bmatrix} \frac{\beta_+ r_- - \beta_- r_+}{\beta_+ - \beta_-} & \frac{r_+ - r_-}{\beta_+ - \beta_-} \\ \frac{\beta_+ \beta_- r_- - \beta_+ \beta_- r_+}{\beta_+ - \beta_-} & \frac{\beta_+ r_+ - \beta_- r_-}{\beta_+ - \beta_-} \end{bmatrix}, \quad (\text{S3})$$

110 where  $r_{\pm} = \frac{1-n_{\pm}}{1+n_{\pm}}$ . Complex Kerr angle can be defined with following expressions as,

$$\theta_K^{yx} = \frac{r_{yx}}{r_{xx}} \quad (\text{S4})$$

111 and

$$\theta_K^{xy} = -\frac{r_{xy}}{r_{yy}}. \quad (\text{S5})$$

112 Approximately, complex Kerr angles can be written in terms of off-diagonal permittivity tensor  
113 component as,

$$\theta_K^{yx} \approx \beta_+ \frac{2(n_+ - n_-)}{(1-n_+)(1+n_-)} = \frac{-2\varepsilon_{yx}}{(n_x + n_y)(1-n_x)(1+n_y)} \quad (\text{S6})$$

114 and

$$\theta_K^{xy} \approx \frac{1}{\beta_-} \frac{2(n_+ - n_-)}{(1+n_+)(1-n_-)} = \frac{2\varepsilon_{xy}}{(n_x + n_y)(1+n_x)(1-n_y)}. \quad (\text{S7})$$

115

116 **S6. Jones matrix formalism for polarization angle dependent nonlinear Kerr rotation.**

117 We analyzed current-induced Kerr signals by adopting Jones matrix formalism. Our optical  
118 Kerr effect measurement can be written as,

$$\begin{pmatrix} E_{out}^x(j_c) \\ E_{out}^y(j_c) \end{pmatrix} = M_{\lambda/2} \left( 22.5^\circ + \frac{\phi}{2} \right) M_{\lambda/4}(\phi) R(j_c) M_{\lambda/2} \left( \frac{\phi}{2} \right) \begin{pmatrix} E_{in}^x \\ E_{in}^y \end{pmatrix} \quad (S8)$$

and

$$\begin{pmatrix} E_{out}^x(j_c) \\ E_{out}^y(j_c) \end{pmatrix} = M_{\frac{\lambda}{2}} \left( 22.5^\circ + \frac{\phi}{2} \right) R(j_c) M_{\frac{\lambda}{2}} \left( \frac{\phi}{2} \right) \begin{pmatrix} E_{in}^x \\ E_{in}^y \end{pmatrix}, \quad (S9)$$

119 where  $E_{in}^i$  ( $E_{out}^i$ ) is initial (final) electric field of light with a polarization along  $i$ -direction  
120 and  $j_c$  is electric current density. Equation S1 is with a quarter-wave plate and eq. S2 is  
121 without the plate. Optical elements of Jones matrix are following as,

$$\text{Half-wave plate: } M_{\lambda/2}(\phi) = e^{-i\frac{\pi}{2}} \begin{pmatrix} \cos^2\phi - \sin^2\phi & 2\cos\phi\sin\phi \\ 2\cos\phi\sin\phi & \sin^2\phi - \cos^2\phi \end{pmatrix}, \quad (S10)$$

$$\text{Quarter-wave plate: } M_{\lambda/4}(\theta) = e^{-i\frac{\pi}{4}} \begin{pmatrix} \cos^2\phi + i\sin^2\phi & (1-i)\cos\phi\sin\phi \\ (1-i)\cos\phi\sin\phi & \sin^2\phi + i\cos^2\phi \end{pmatrix}, \quad (S11)$$

$$\text{Reflection matrix: } R(j_c) = \begin{pmatrix} r_{xx} & r_{xy} \\ r_{yx} & r_{yy} \end{pmatrix}, \quad (S12)$$

122 where  $\theta$  is the orientation of the fast axis of optical elements with respect to the  $x$ -axis.

123 Balanced detection with an application of electric current can be described as,

$$\frac{|E_{out}^x(j_c)|^2 - |E_{out}^y(j_c)|^2}{E_0^2} = \frac{\Delta I(j_c)}{I_0}, \quad (S13)$$

124 where  $E_0^2 = |E_{out}^x|^2 + |E_{out}^y|^2$ . Finally, the intensity from lock-in detection can be written as

$$I_{LIA}(j_c) = \frac{\Delta I(j_c)}{I_0} - \frac{\Delta I(j_c=0)}{I_0} \quad (S14)$$

125 Total permittivity tensor can be written in terms of first- and third-order permittivity  
126 components as,

$$\tilde{\epsilon} = \begin{pmatrix} \tilde{\epsilon}_{xx} & \tilde{\epsilon}_{xy} \\ \tilde{\epsilon}_{yx} & \tilde{\epsilon}_{yy} \end{pmatrix}, \quad (S15)$$

127 where  $\tilde{\epsilon}_{ij} = \epsilon_{ij} + \sum_{m,n}^{i,j} \epsilon_{imnj} E_m E_n$ . For example,  $\tilde{\epsilon}_{xy} = \epsilon_{xy} + \epsilon_{xxx} E_x E_x + 2\epsilon_{xxy} E_x E_y +$   
128  $\epsilon_{xyy} E_y E_y$ , where  $E_x = E_0 \cos(\phi)$  and  $E_y = E_0 \sin(\phi)$ .

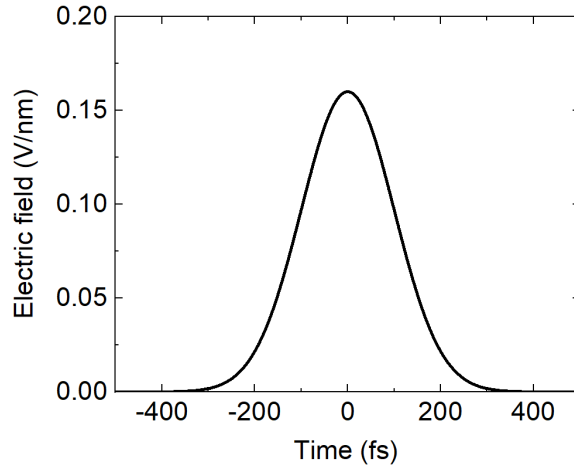
129 For grazing angle incident experiments, we rotate  $3 \times 3$  permittivity tensor  $\tilde{\epsilon}$  with respect to  
130  $x$ - or  $y$ - axis with a weighting factor  $\cos^2(\psi)$  incorporating the optical fluence decrease.

131 Rotation of permittivity tensor with a rotation angle  $\psi$  can be represented as,

$$\tilde{\epsilon}'(\psi) = A(-\psi)\tilde{\epsilon}A^T(-\psi), \quad (\text{S16})$$

where

$$A(\psi) = \begin{pmatrix} \cos(\psi) & -\sin(\psi) \\ \sin(\psi) & \cos(\psi) \end{pmatrix}. \quad (\text{S17})$$



132

133 Figure S6. Gaussian-shaped time profile of pulsed laser estimation.

134

135 For extracting susceptibility tensor component values, we estimate the peak electric field of  
 136 pulsed laser with simple manipulation. Intensity of pulsed laser in time-domain can be written  
 137 as,

$$I(t) = I_{\text{peak}} \text{Exp} \left[ -\left( \frac{t}{\tau} \right)^2 \right], \quad (\text{S18})$$

138 where  $I_{\text{peak}}$  is peak intensity and  $\tau$  is pulse width. We use pre-parameters that beam power is  
 139 5 mW, pulse width is 100 fs, repetition rate is 80 MHz, beam radius is 1  $\mu\text{m}$ , and refractive  
 140 index of WTe<sub>2</sub> is 3.3. By using relation between intensity and electric field,  $I_{\text{peak}} = \frac{cn\epsilon_0}{2} |E_0|^2$ ,  
 141 the peak intensity  $I_{\text{peak}}$  can be converted into the peak electric field  $E_0$  and its time profile is  
 142 shown in Fig. S6. Finally, we calculate that  $I_{\text{peak}} = 1.1 \times 10^{14} \text{ W/m}^2$  and  $E_0 = 0.16 \text{ V/nm}$ .

143 Finally, we simulate polarization angle dependent Kerr angle and extract third-order  
 144 susceptibility tensor component values as shown in Fig. 4 in main text. Here, we show a  
 145 possible combination of susceptibility tensor component values in Table S1.

146  
147

**Table S1. Extracted fourth-order susceptibility tensor components. Unit of all susceptibility components is  $10^9 \text{pm}^3/\text{V}^3$ .**

$\text{Re}[\chi_{abbbb}^{(3)}]$	-282.1
$\text{Re}[\chi_{bbaaa}^{(3)}]$	703.1
$\text{Im}[\chi_{abbbb}^{(3)}]$	-277.8
$\text{Im}[\chi_{bbaaa}^{(3)}]$	-182.3
$\text{Im}[\chi_{ababb}^{(3)}] + \text{Im}[\chi_{abbab}^{(3)}]$	503.5
$\text{Im}[\chi_{bbbaa}^{(3)}]$	-251.7
$\text{Re}[\chi_{bbaac}^{(3)}]$	3125.0
$\text{Re}[\chi_{abbbc}^{(3)}]$	-104.2

148  
149

## S7. Symmetry analysis of the photocurrent in view of the crystalline symmetries of WTe<sub>2</sub>.

### *Symmetries of the bulk WTe<sub>2</sub>*

The known atomic structures of three-dimensional WTe<sub>2</sub> include the most stable  $T_d$  phase and a meta-stable  $T'$  phase. The  $T_d$  belongs to an orthorhombic space group  $Pmn2_1$  (# 31). The absence of inversion symmetry is a key feature that allows for the occurrence of the Weyl semimetal phase. This space group is generated by a mirror reflection  $m_a$  and a glide mirror reflection  $g_b = \{m_b|1/2, 0, 1/2\}$ , where  $g_b$  is a mirror operation followed by a translation by  $a/2+c/2$ . On the other hand, WTe<sub>2</sub> is also found in the  $T'$  phase, corresponding to a monoclinic  $P12_1/m1$  space group ( $P2_1/m$ , # 11). Notably, it preserves inversion symmetry  $\mathcal{P}$  and a mirror reflection  $\{m_b|0, 1/2, 0\}$ . Both phases are known to be non-magnetic, thereby preserving time-reversal symmetry  $\mathcal{P}$ . WTe<sub>2</sub> in the non-centrosymmetric  $T_d$  phase is of our interest in the present work, hosting the Weyl semimetal phase.

Symmetry transformations of  $v_\alpha$ ,  $\partial_\beta$ , and  $\Omega_{\alpha\beta}$ .

The Berry curvature  $\Omega_{\alpha\beta}$ , the corresponding pseudo vectors  $\mathcal{B}_\gamma \equiv \epsilon_{\alpha\beta\gamma}\Omega_{\alpha\beta}/2$ , group velocities  $v_\alpha = \frac{1}{\hbar}\partial_\alpha E_k$ , where  $E_k$  is the energy and  $\frac{\partial}{\partial k_\alpha} \equiv \partial_\alpha$  is the momentum derivatives, conform the following transformation rules, where  $\alpha \equiv a, b$ , and  $c$ .

Under inversion  $\mathcal{P}$ :

$$v_\alpha \rightarrow -v_\alpha \quad (\text{S19})$$

$$B(\mathbf{k})_\beta \rightarrow B(-\mathbf{k})_\beta \quad (\text{S20})$$

$$\partial_\gamma \rightarrow -\partial_\gamma \quad (\text{S21})$$

Under time-reversal  $\mathcal{T}$ :

$$v_\alpha \rightarrow -v_\alpha \quad (\text{S22})$$

$$B(\mathbf{k})_\beta \rightarrow -B(-\mathbf{k})_\beta \quad (\text{S23})$$

$$\partial_\gamma \rightarrow -\partial_\gamma \quad (\text{S24})$$

176 Under mirror (glide) reflection  $m_b(g_b)$ :

177

$$v_\alpha \rightarrow (-1)^{\delta_{b\alpha}} v_\alpha \quad (\text{S25})$$

$$B(\mathbf{k})_\beta \rightarrow (-1)^{\delta_{b\beta}} B(-\mathbf{k})_\beta \quad (\text{S26})$$

$$\partial_\gamma \rightarrow (-1)^{\delta_{b\gamma}} \partial_\gamma \quad (\text{S27})$$

178

179

### *Second-order photo-response*

180 The current-induced nonlinear Kerr effect arises in a time-reversal symmetric system as a  
 181 consequence of a higher-order nonlinear response to an applied field of the light. Here, we  
 182 show that the crystalline symmetries of WTe<sub>2</sub> suppress the lower-order responses to the applied  
 183 field, and the fourth-order nonlinear response arises as the dominant contribution to the  
 184 nonlinear Hall effect that we observed in WTe<sub>2</sub>. The photo-current, which is responsible for the  
 185 observed Kerr effect, is derived using the Boltzmann semi-classical approach with the  
 186 relaxation time in literatures. Here, we used the nonlinear photocurrent expression of Parker,  
 187 Morimoto, Orenstein, and Moore<sup>4</sup> and apply the symmetries of WTe<sub>2</sub>. Let us first consider the  
 188 second-order photo-response to the incident field of the light  $\mathcal{E}(t) = \mathcal{E}e^{i\omega t} + \mathcal{E}^*e^{-i\omega t}$  and  
 189 the nearly-static in-plane displacement field  $\mathbf{D}$  that generates an electric polarization

$$\mathbf{J}_\mu^{(2)}(\omega) = \sum_p \sigma_{\mu\alpha\beta}^{(2)}(\omega) \mathbf{D}_{p(\alpha)} \mathcal{E}_{p(\beta)}(\omega) \quad (\text{S28})$$

190 Here,  $p$  is a permutation and the nonlinear conductivity  $\sigma_{\mu\alpha\beta}(\omega)$  is given by

$$\sigma_{\mu\alpha\beta}^{(2)} = \frac{e^3}{\hbar^2} \int \frac{d^3\mathbf{k}}{(2\pi)^3} f_{\text{FD}} \left( -i \frac{\partial_\alpha \partial_\beta v_\nu}{\omega^2} - \frac{\partial_\alpha \Omega_{\mu\beta}}{\tilde{\omega}} \right). \quad (\text{S29})$$

191 Here,  $\tilde{\omega} = \omega + i/\tau$ , where  $\omega$  is the angular frequency of light and  $\tau$  is the relaxation time.  
 192 The integration is done over the first Brillouin zone. The first (second) term is odd (even) under  
 193  $\mathcal{T}$ , thus vanishing (surviving) in a time-reversal symmetric system. The point group of the  $T_d$   
 194 phase is  $mm2$ , comprising two mirrors  $m_a$  and  $m_b$ . Here, we set  $\hat{a} \parallel \hat{x}$ ,  $\hat{b} \parallel \hat{y}$ , and  $\hat{c} \parallel \hat{z}$ . The  
 195 crystalline direction  $\mathbf{a}$  ( $\mathbf{b}$ ) corresponds to the shorter (longer) lattice constant of the primitive  
 196 unit cell. Under the  $mm2$  symmetries,  $\Omega_{ab}(\mathbf{k})$  is an even function of  $\mathbf{k}$ , and thus, together  
 197 with  $\mathcal{T}$ ,  $\Omega_{ab}=0$ . The only possible non-zero components  $\Omega_{ac}$  and  $\Omega_{bc}$  are odd (even)  
 198 functions under  $m_a$  ( $m_b$ ) and  $m_b$  ( $m_a$ ), respectively. Therefore,  $\partial_a \Omega_{bc}$  and  $\partial_b \Omega_{ac}$  vanish as  
 199 they are odd under  $m_a$  and  $m_b$ , respectively. However,  $\partial_a \Omega_{ac}$  and  $\partial_b \Omega_{bc}$  survive as they are  
 200 even under both  $m_b$  and  $m_a$ . As a consequence, the (linear) Kerr effect occurs only via the Berry  
 201 curvature dipole components  $\partial_a \Omega_{ac}$  and  $\partial_b \Omega_{bc}$ , if any. These components are, in principle,

202 allowed upon the oblique incidence of the light, resulting in the Kerr rotation that is  
 203 independent of the power of light source in the case where the displacement field direction is  
 204 perpendicular to the in-plane component of the light field. However, our experimental results  
 205 show that the Kerr rotation from these components is negligible. We believe that this captures  
 206 a non-perturbation nature of the nonlinear optical response, potentially attributed to the high  
 207 intensity of the laser source.

208

209

### *Third-order photo-response*

210 Having discussed the second nonlinear response, we now move to the third-order response in  
 211 its first-harmonic generation:

$$J_{\mu}^{(3)}(\omega) = \sum_p \sigma_{\mu\alpha\beta\gamma}^{(3)}(\omega) \mathcal{E}_{p(\alpha)}(\omega) \mathcal{E}_{p(\beta)}^*(-\omega) \mathcal{E}_{p(\gamma)}(\omega) \quad (\text{S30})$$

212 Note that the polarization in the first-harmonic generation has only the terms with zeroth or  
 213 square-order of  $\mathbf{D}$ . We ruled out the cases of the square-order of  $\mathbf{D}$  as  $D \ll \mathcal{E}$ . The  
 214 corresponding Hall conductivity tensor again can be obtained from the Boltzmann equation  
 215 approach by<sup>4</sup>

$$\sigma_{\mu\alpha\beta\gamma}^{(3)}(\omega) = \frac{e^4}{\hbar^3} \int \frac{d^3\mathbf{k}}{(2\pi)^3} f_{\text{FD}} \left( -i \frac{\partial_{\alpha} \partial_{\beta} \partial_{\gamma} v_{\mu}}{2\tilde{\omega}\tilde{\omega}^2} - \frac{\partial_{\alpha} \partial_{\beta} \Omega_{\mu\gamma}}{\tilde{\omega}^2} \right), \quad (\text{S31})$$

216 where  $\tilde{n}\tilde{\omega} = n\omega + i/\tau$ , for any integer  $n$ . The third-order conductivity comprises (first)  
 217 Drude-like and (second) Berry curvature quadrupole terms. Both terms are essentially  
 218 forbidden by  $2mm$  and  $\mathcal{T}$  since the first ‘‘Drude-like’’ term is odd under either  $m_a$  or  $m_b$  and  
 219 the second Berry quadrupole term is odd under  $\mathcal{T}$ .

220

221

### *Fourth-order photo-response*

222 The symmetry allowed contribution first appears in the fourth-order response. The fundamental  
 223 first-harmonic generation of fourth-order photo-response can be obtained<sup>4</sup>

$$J_{\mu}^{(4)}(\omega) = \sum_p \sigma_{\mu\alpha\beta\gamma\delta}^{(4)}(\omega) \mathbf{D}_{p(\alpha)} \mathcal{E}_{p(\alpha)}(\omega) \mathcal{E}_{p(\gamma)}^*(-\omega) \mathcal{E}_{p(\delta)}(\omega) \quad (\text{S32})$$

224 where

$$\sigma_{\mu\alpha\beta\gamma\delta}^{(4)}(\omega) = \frac{e^5}{\hbar^4} \int \frac{d^3\mathbf{k}}{(2\pi)^3} f_{\text{FD}} \left( -i \frac{\partial_{\alpha} \partial_{\beta} \partial_{\gamma} \partial_{\delta} v_{\mu}}{3\tilde{\omega}2\tilde{\omega}\tilde{\omega}^2} - \frac{\partial_{\alpha} \partial_{\beta} \partial_{\gamma} \Omega_{\mu\delta}}{2\tilde{\omega}\tilde{\omega}^2} \right), \quad (\text{S33})$$

225 The first ‘‘Drude-like’’ term vanishes under  $\mathcal{T}$  as it is an odd function of  $\mathbf{k}$ . The second terms,  
 226 related with the Berry hexapole, have four types of components that survive under the  
 227 symmetry operations of  $2mm$  and  $\mathcal{T}$ , which are

$$\partial_a \partial_a \partial_a \Omega_{ca} \quad (\text{S34})$$

$$\partial_a \partial_b \partial_b \Omega_{ca} \quad (\text{S35})$$

$$\partial_a \partial_a \partial_b \Omega_{cb} \quad (\text{S36})$$

$$\partial_b \partial_b \partial_b \Omega_{cb} \quad (\text{S37})$$

228 Note that we assume  $\mathbf{E}$  and  $\mathbf{D}$  are all in-planar fields and keep only the zeroth and first power  
 229 of  $\mathbf{D}$  as  $D \ll \mathcal{E}$ . These Berry curvature hexapole components in forth-order nonlinear  
 230 response are all even under  $m_a$ ,  $m_b$ , and  $\mathcal{T}$ . We expect that these are dominantly contributing  
 231 terms in our experiments upon the exertion of oblique incidence light on the bulk WTe<sub>2</sub>. We  
 232 converted the expression for  $\sigma_{\mu\alpha\beta\gamma\delta}^{(4)}(\omega)$  to the expression for  $\chi_{\mu\alpha\beta\gamma\delta}^{(4)}(\omega)$ , equation (4) of the  
 233 main text, using the relationship between the off-diagonal dielectric constant and the Hall  
 234 conductivity,  $\varepsilon_{\mu\delta} = \frac{1}{i\varepsilon_0\omega} \sigma_{\mu\delta}$ .

235

- 236 1. Kim, M. *et al.* Determination of the thickness and orientation of few-layer tungsten ditelluride using  
237 polarized Raman spectroscopy. *2D Mater.* **3**, 034004 (2016).
- 238 2. Song, Q. *et al.* The in-plane anisotropy of WTe<sub>2</sub> investigated by angle-dependent and polarized Raman  
239 spectroscopy. *Sci. Rep.* **6**, 29254 (2016).
- 240 3. Putz, S., Gmitra, M. & Fabian, J. Anisotropic optical properties of Fe/GaAs(001) nanolayers from first  
241 principles. *Phys. Rev. B* **90**, 045315 (2014).
- 242 4. Parker, D. E., Morimoto, T., Orenstein, J. & Moore, J. E. Diagrammatic approach to nonlinear optical  
243 response with application to Weyl semimetals. *Phys. Rev. B* **99**, 045121 (2019).